Shear-induced fluid-tracer diffusion in a semidilute suspension of spheres

doi: 10.1103/PhysRevE.77.041402

Shear-induced fluid-tracer diffusion in a semidilute suspension of spheres

Takuji Ishikawa and Takami Yamaguchi
Department of Bioengineering and Robotics, Tohoku University, 6-6-01, Aoba, Aramaki, Aoba-ku, Sendai 980-8579, Japan
(Received 7 January 2008; published 14 April 2008)

We calculated tracer diffusion in a sheared suspension of non-Brownian rigid spheres and propose a numerical method based on a boundary element method and Stokesian dynamics method. We present details of the numerical method and examine the accuracy of the method. The limitation of semidiluteness is due to the accuracy of the tracer velocity calculation. The results show that the diffusivity of fluid tracers is greater than that of suspended spheres in the semidilute regime. The diffusivity of the velocity gradient direction is about threefold greater than that in the vorticity direction. Simple scaling demonstrates that the diffusivity of fluid tracers increases with the square of the volume fraction of spheres in the semidilute regime, which is confirmed numerically.

DOI: 10.1103/PhysRevE.77.041402 PACS number(s): 82.70.Kj, 66.10.C−, 83.10.−y, 47.27.W−

I. INTRODUCTION

The diffusion of chemical substances in a suspension of micron-scale particles is an important phenomenon. For example, the mass transport of various substances such as oxygen, CO_2, and low-density lipoprotein in the bloodstream is often discussed in the field of medical engineering because of the physiological and pathological importance of these processes. These substances are dispersed not only by Brownian diffusion, but also by the micron-scale flow field generated by blood cells. The diffusivity of platelets increases markedly compared to Brownian diffusivity because of the micron-scale flow field [1]. Another example is a suspension of microorganisms, which appears in plankton blooms in the ocean, bioreactors for food and medicine production, and churning colloid suspensions of the chime in the lower intestine. In such suspensions, both the motion and the population of microorganisms are strongly influenced by nutrient transport in the suspension. Wu and Libchaber [2] demonstrated experimentally that the diffusivity of inert tracer particles in a suspension of *Escherichia coli* is increased by a thousandfold as compared to Brownian diffusivity because of the flow field generated by the cells' swimming motion.

When micron-scale particles are exposed to a simple shear flow, the motion of particles generates a micron-scale flow field around them, which leads to mixing of the particles and fluid. The shear-induced diffusion of suspended rigid spheres in a fluid has been investigated intensively. Batchelor and Green [3] analyzed the hydrodynamic interactions between two non-Brownian spheres in a shear flow and showed that no displacement perpendicular to the flow direction is generated in the two-sphere interaction. In a dilute suspension, shear-induced diffusion does appear in all directions, as reported by Acrivos *et al.* [4], because other particles break the symmetry of the two-sphere interaction. The shear-induced diffusion of non-Brownian and Brownian spheres in a concentrated suspension has been investigated numerically by Acrivos and co-workers [5–7] and by Brady and co-workers [8–12]. These studies demonstrated that the nonzero components of the diffusion tensor are strongly dependent on the volume fraction of the spheres. Experimental investigations of the shear-induced diffusion have also been reported [13,14]. The former experimental results were compared with analytical and numerical results by Sierou and Brady [12] (cf. Figs. 4 and 5 in their paper), although the results indicate a large degree of deviation among different studies. This deviation may be due to experimental differences, such as those caused by difficulties in accurately tracking particles in a concentrated suspension, having spheres without an electric charge, or surface roughness.

Although an important phenomenon, few studies have described shear-induced fluid-tracer diffusion in a suspension of spheres. Zarraga and Leighton [15], and Abbas *et al.* [16] numerically investigated shear diffusivity in bidisperse suspensions under Stokes flows. In the limit where the size ratio between the small and large spheres is very small, the diffusivity of small spheres may be similar to that of fluid tracers (although they did not investigate it). In addition, one experimental study had been conducted in which tracer particles 31.5 μm in diameter were tracked in a suspension of spheres 325 μm in diameter [17]. Tracer diffusivity was observed in just two cases, $c=0.3$ and 0.4, where c is the volume fraction of large spheres. In their experiments, the tracer diffusivity was about 0.7 times the particle diffusivity. However, this tendency was different from that seen in the present study in a semidilute suspension. In the dilute limit, we clearly showed that the tracer diffusivity is greater than the particle diffusivity (cf. Sec. V). The difference in tendency may have been due to differences in the volume fractions used in the two studies, but the details of tracer diffusion are still not well understood. Experimentally, tracking small particles continuously in a sheared suspension of large particles is very difficult, but no suitable numerical method to address this problem has yet been proposed.

Here, we calculate tracer diffusion in a sheared suspension of non-Brownian rigid spheres. Fluid tracers are assumed to be infinitely small, but do not show any Brownian motion—i.e., ideal particles moving with the fluid velocity—although practical fluid, such as water, shows self-diffusion due to Brownian motion [18]. This treatment corresponds to infinitely large Péclet number flow for the fluid tracers. (In Sec. V, we discuss effects of the self-diffusion.) In order to solve this problem, we propose a numerical method based on a boundary element method (BEM) [19] and Stokesian dy-

namics method (SDM) [20]. This method is a hybrid of our BEM study [21] and our SDM studies [22–24]. Details of the numerical method are explained in Sec. II. The accuracy of the numerical method is checked in Sec. III by comparing the velocity fields between the present method and BEM. In Sec. IV, we show shear-induced tracer diffusion in a semidilute suspension of non-Brownian spheres. The limitation of semidiluteness comes from the present numerical method, specifically in accurately calculating the tracer velocity. In Sec. V, we compare the present results with previous results and discuss the scaling of diffusivity.

II. METHODS

The Stokesian dynamics simulation method for computing the hydrodynamic interactions among an infinite suspension of spheres, in the absence of Brownian motion and at negligible particle Reynolds number, was developed by Brady and Bossis [20]. We used the same method for calculating the motions of neutrally buoyant spheres in a suspension, which are explained briefly in Sec. II A. Numerical methods for simulating fluid-tracer motions are derived here and are explained in detail in Sec. II B. The numerical methods for simulating sphere motions are valid even for a concentrated suspension of spheres, whereas those for fluid-tracer motions are valid only under a semidilute regime. Thus, we restricted ourselves to simulating a semidilute suspension.

A. Equations for motion of suspended spheres

At negligible particle Reynolds number, the motions of N spheres replicated periodically in three-dimensional space can be given as (cf. [20,24])

$$\begin{pmatrix} \boldsymbol{F} \\ \boldsymbol{L} \\ \boldsymbol{S} \end{pmatrix} = [\boldsymbol{R}^{\mathrm{far}} - \boldsymbol{R}_{2B}^{\mathrm{far}} + \boldsymbol{R}_{2B}^{\mathrm{near}}] \begin{pmatrix} \boldsymbol{U} - \langle \boldsymbol{u} \rangle \\ \boldsymbol{\Omega} - \langle \boldsymbol{\omega} \rangle \\ -\langle \boldsymbol{E} \rangle \end{pmatrix}, \tag{1}$$

where $\boldsymbol{F}$, $\boldsymbol{L}$, and $\boldsymbol{S}$ are the force, torque, and stresslet exerted by a sphere on the fluid, respectively; $\boldsymbol{U}$ and $\boldsymbol{\Omega}$ are the translational and rotational velocities of a sphere; $\langle \boldsymbol{u} \rangle$ and $\langle \boldsymbol{\omega} \rangle$ are the translational and rotational velocities of the imposed flow, respectively; and $\langle \boldsymbol{E} \rangle$ is the imposed rate of the strain tensor. $\boldsymbol{R}^{far}$ is the far-field contribution of the grand resistance matrix, which is the inversion of the far-field contribution of the grand mobility matrix; i.e., $\boldsymbol{R}^{far} = \{\boldsymbol{M}^{far}\}^{-1}$. $\boldsymbol{M}^{far}$ is derived from the Faxén laws for the force, torque, and stresslet for a sphere, in which the disturbed flow field is expressed in terms of the multipole expansion of other spheres. The infinite extent of a suspension is evaluated by Ewald summation [25]. As discussed by Durlofsky *et al.* [26], inverting the Ewald-summed mobility matrix sums an infinite number of reflected interactions among an infinite number of particles, and it is therefore a true many-body approximation to the resistance matrix. Therefore, this method is applicable to any volume fraction of particles. $\boldsymbol{R}^{far}$ still lacks near-field interactions because they are reproduced only when all of the multipoles are included. To include the near-field interactions, we follow the method of Durlofsky *et al.* [26] and add near-field multipoles in a pairwise additive fashion: $\boldsymbol{R}_{2B}^{far}$ is the far-field two-body resistance matrix and $\boldsymbol{R}_{2B}^{near}$ is the near-field two-body resistance matrix.

B. Equations for a fluid-tracer motion

A flow field external to N spheres replicated periodically in three-dimensional space can be given in the integral form using single-layer potential [19]:

$$u_i(\boldsymbol{x}) - \langle u_i(\boldsymbol{x}) \rangle = -\frac{1}{8\pi\mu} \sum_{\alpha=1}^{N} \int_{A_\alpha} J_{ij}(\boldsymbol{x} - \boldsymbol{y}) q_j(\boldsymbol{y}) dA_y, \tag{2}$$

where $\boldsymbol{u}$ is the velocity, μ is the viscosity, and the angular brackets $\langle \cdots \rangle$ indicate the suspension average. $\boldsymbol{J}$ is the Green's function for a triply periodic lattice, $\boldsymbol{q}$ is the single-layer potential, and A is the surface of a particle. $\boldsymbol{J}$ is evaluated by Ewald summation on the lattice and reciprocal lattice of image points, as derived by Beenakker [25]:

$$J_{ij}(\boldsymbol{r}) = \sum_{\gamma} H_{ij}^{(1)}(\boldsymbol{r}_\gamma) + \frac{8\pi}{V} \sum_{\lambda \neq 0} [H_{ij}^{(2)}(\boldsymbol{k}_\lambda) \cos(\boldsymbol{k}_\lambda \cdot \boldsymbol{r})] - \frac{8\xi}{\sqrt{\pi}} \delta_{ij} \delta(\boldsymbol{r}), \tag{3}$$

$$H_{ij}^{(1)}(\boldsymbol{r}) = \frac{\delta_{ij}}{r} \left\{ \mathrm{erfc}(\xi r) + \frac{e^{-\xi^2 r^2}}{\sqrt{\pi}} (4\xi^3 r^3 - 6\xi r) \right\} + \frac{r_i r_j}{r^3} \left\{ \mathrm{erfc}(\xi r) + \frac{e^{-\xi^2 r^2}}{\sqrt{\pi}} (2\xi r - 4\xi^3 r^3) \right\}, \tag{4a}$$

$$H_{ij}^{(2)}(\boldsymbol{k}) = \left(\frac{\delta_{ij}}{|\boldsymbol{k}|^2} - \frac{k_i k_j}{|\boldsymbol{k}|^4} \right) \left(1 + \frac{|\boldsymbol{k}|^2}{4\xi^2} + \frac{|\boldsymbol{k}|^4}{8\xi^4} \right) \exp\left(-\frac{|\boldsymbol{k}|^2}{4\xi^2} \right), \tag{4b}$$

where ξ is the convergence parameter, $\boldsymbol{\delta}$ is the unit isotropic tensor, V is the volume of each unit cell, and $r = |\boldsymbol{r}|$. The lattice points are $\boldsymbol{x}_\gamma$ and $\boldsymbol{r}_\gamma = \boldsymbol{r} - \boldsymbol{x}_\gamma$; $\boldsymbol{k}_\lambda$ are the reciprocal lattice vectors defined such that $\boldsymbol{x}_\gamma \cdot \boldsymbol{k}_\lambda$ is an integer multiple of 2π. The first sum in the right-hand side (RHS) of (3) converges rapidly in real space, while the second converges rapidly in reciprocal space.

The RHS of Eq. (2) can be expanded in moments about the center of each particle with radius a as follows (see [20,24]):

$$u_i(\boldsymbol{x}) - \langle u_i(\boldsymbol{x}) \rangle = \frac{1}{8\pi\mu} \sum_{\alpha=1}^{N} \left[\left(1 + \frac{a^2}{6} \nabla^2 \right) J_{ij} F_j^\alpha + R_{ij} L_j^\alpha + \left(1 + \frac{a^2}{10} \nabla^2 \right) K_{ijk} S_{jk}^\alpha + \nabla_k \nabla_l J_{ij} Q_{klj}^\alpha + \cdots \right], \tag{5}$$

where $\boldsymbol{Q}$ is the irreducible quadrupole of the single-layer potential. The propagators are given as follows:

$$R_{ij} = \epsilon_{lkj}\frac{1}{4}(\nabla_k J_{il} - \nabla_l J_{ik}), \quad K_{ijk} = \frac{1}{2}(\nabla_k J_{ij} + \nabla_j J_{ik}), \quad (6)$$

where ϵ is the unit-alternating isotropic tensor.

If a suspension is under the semidilute regime, most of the interactions between spheres are pairwise. Thus, it is possible to assume that a fluid tracer may have a maximum of two spheres in its near field with the other spheres in the far field. When spheres are in the far field, high multipoles in Eq. (5) decay very rapidly. Therefore, it may be sufficiently accurate to take part in multipoles up to the stresslet, which are part of the problem in solving Eq. (1). If a sphere exists in the near field, however, all the multipoles contribute to the velocity field and its effect cannot be simplified by the small number of multipoles. Thus, it is necessary to calculate an infinite number of multipoles for spheres in the near field, although we calculate up to the stresslet for the far field. The maximum number of spheres in the near-field is assumed to be two, which defines semidiluteness.

By assuming semidiluteness, Eq. (5) can be approximated as

$$\begin{aligned} u_i(\boldsymbol{x}) - \langle u_i(\boldsymbol{x})\rangle = {} & \frac{1}{8\pi\mu}\sum_{\alpha=1}^{N}\left[\left(1+\frac{a^2}{6}\nabla^2\right)J_{ij}F_j^\alpha + R_{ij}L_j^\alpha + K_{ijk}S_{jk}^\alpha \right. \\ & \left. + \nabla_k\nabla_l J_{ij}Q_{klj}^\alpha\right] - \frac{1}{8\pi\mu} \\ & \times \sum_{\alpha=1}^{2}\sum_{m=2}^{\infty}{}' \int_{A_\alpha}\left[\frac{(-1)^m}{m!}\frac{\partial^m}{\partial k_1\cdots\partial k_m}J'_{ij}\right. \\ & \left. \times (y_{k_1} - x_{k_1}^\alpha)\cdots(y_{k_m} - x_{k_m}^\alpha)q_j(\boldsymbol{y})\right]dA_y, \end{aligned} \quad (7)$$

where N_{near} is the number of spheres in the near field ($N_{near} \leq 2$) and J'_{ij} is the Oseen tensor given as

$$J'_{ij}(\boldsymbol{r}) = \frac{\delta_{ij}}{r} + \frac{r_i r_j}{r^3}. \quad (8)$$

The contribution from an infinite number of spheres in the far field is calculated in the first summation on the RHS of (7). The multipoles exerted on the fluid can be obtained up to the stresslet from Eq. (1), and the irreducible quadrupole is approximated, as explained in Durlofsky *et al.* [26], as

$$Q_{klj}^\alpha = \frac{a^2}{10}c\langle F_m\rangle\left(\delta_{km}\delta_{jl} + \delta_{lm}\delta_{kj} - \frac{2}{3}\delta_{kl}\delta_{jm}\right), \quad (9)$$

where c is the volume fraction of particles. The contribution of two spheres in the near field is calculated by summing all the multipoles. The first few multipoles are added in the first summation on the RHS of (7), while the rest of the multipoles are added in the second summation. The prime on the second sum indicates that the quadrupole contribution already added in the first summation is excluded when $m=2$.

To simplify the explanation, let $N_{near}=2$ and let background shear flow be applied. Considering the linearity of the Stokes flow, the mth multipole exerted on the sphere in the near field can be divided into three simpler multipoles: (a) mth multipole due to translational and rotational motion of two spheres in a fluid otherwise at rest, (b) mth multipole due to the background shear flow without translational and rotational motion of spheres, and (c) mth multipole due to background disturbance flow field generated by the other spheres in the far field, without translational and rotational motion. The mth multipole in (c) can be calculated by the Faxén laws and decays rapidly with $r^{-(m+2)}$ when a sphere is force free. Thus, we neglect the contribution of (c) for high multipoles—i.e., $m \geq 2$. The mth multipole in (a) and (b) can be calculated by considering only two-sphere interactions because no disturbance flow field is generated by the other particles. Therefore, it is computationally efficient to build a database for high multipoles prior to the simulation, and thus it is possible to avoid calculating two-sphere interactions at every time step in the simulation.

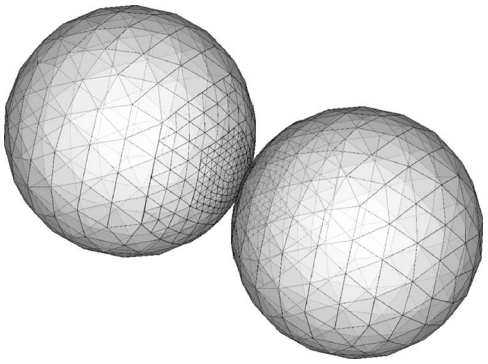

FIG. 1. Boundary elements on the surfaces of spheres, where smaller triangles are generated near the contact region. The total number of the mesh is 590 per sphere.

The interaction between two swimming spheres has been investigated previously [21], and we used the same method here in compiling a database. We employed the boundary element method, in which the boundary integral equation is solved discretely on 590 triangular elements per sphere surface (Fig. 1). The velocity field around the two spheres can be calculated by the boundary integral equation, which should be the sum of the velocity due to first few multipoles and the velocity due to the rest of the multipoles. Thus, the velocity can be expressed as

$$\begin{aligned} u_i(\boldsymbol{x}) = {} & -\frac{1}{8\pi\mu}\sum_{\alpha=1}^{2}\int_{A_\alpha} J'_{ij}(\boldsymbol{x}-\boldsymbol{y})q_j(\boldsymbol{y})dA_y \\ = {} & \frac{1}{8\pi\mu}\sum_{\alpha=1}^{2}\left[\left(1+\frac{a^2}{6}\nabla^2\right)J_{ij}F_j^\alpha + R_{ij}L_j^\alpha + K_{ijk}S_{jk}^\alpha \right. \\ & \left. + \nabla_k\nabla_l J_{ij}Q_{klj}^\alpha\right] - \frac{1}{8\pi\mu} \\ & \times \sum_{\alpha=1}^{2}\sum_{m=2}^{\infty}{}' \int_{A_\alpha}\left[\frac{(-1)^m}{m!}\frac{\partial^m}{\partial k_1\cdots\partial k_m}J'_{ij}\right. \\ & \left. \times (y_{k_1} - x_{k_1}^\alpha)\cdots(y_{k_m} - x_{k_m}^\alpha)q_j(\boldsymbol{y})\right]dA_y. \end{aligned} \quad (10)$$

The first line in Eq. (10) is the velocity obtainable by the

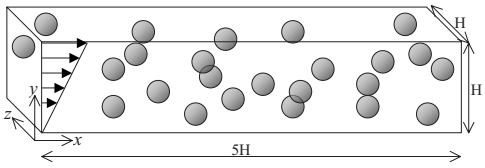

FIG. 2. Schematic representation of the computed system. Background shear flow is applied to a suspension of spheres in a hexahedral unit cell. (a) Schematic representation of the computed system. (b) Comparison of the velocity distribution between the present method (*present*) and the exact solution (*exact*).

boundary integral method, $\boldsymbol{u}_{BEM}$; the second line is the velocity due to low multipoles, $\boldsymbol{u}_{LMP}$; and last two lines are the velocity due to high multipoles, $\boldsymbol{u}_{HMP}$, which we intend to use to build a database. In obtaining $\boldsymbol{u}_{BEM}$ very close to the surface of a sphere, we interpolate it using $\boldsymbol{u}$ on the sphere's surface, which is given as a boundary condition, and $\boldsymbol{u}_{BEM}$ near the point. $\boldsymbol{u}_{HMP}$ can be calculated as $\boldsymbol{u}_{BEM}-\boldsymbol{u}_{LMP}$, and so we compiled a database of $\boldsymbol{u}_{HMP}$ for various translational and rotational motions as well as for any direction of shear flow. As the database for $N_{near}=1$ and 0 is straightforward, we have omitted detailed explanations. In this study, we employed a threshold distance of 4.0 for approximation of far-field interactions. Thus, the velocity disturbance due to spheres farther than 4.0 to a fluid tracer is calculated by the multipoles. In summary, to determine the velocity of a fluid particle, Eq. (7) is calculated using the results of Eq. (1) and the database of $\boldsymbol{u}_{HMP}$.

C. Numerical methods

We calculate the motion of interacting spheres and fluid-tracer motion in a background shear flow: i.e.,

$$\langle \boldsymbol{E} \rangle = \frac{\dot{\gamma}}{2}\begin{pmatrix} 0 & 1 & 0 \\ 1 & 0 & 0 \\ 0 & 0 & 0 \end{pmatrix}, \quad \langle \boldsymbol{\omega} \rangle = -\frac{\dot{\gamma}}{2}(0,0,1), \tag{11}$$

where $\dot{\gamma}$ is the shear rate. The maximum volume fraction of particles used in this study is $c=0.175$. Note that the probability of a fluid tracer having three or more spheres in its near field is $\mathcal{O}(c^3)$. The computational region is a hexahedron with side H in the y and z directions and $5H$ in the x direction as shown in Fig. 2. A suspension of infinite extent is expressed by the periodic boundary conditions, and the interactions among an infinite number of particles are calculated by the Ewald summation over two layers on the real- and reciprocal-space lattices. The convergence parameter ξ in the Ewald sum is set as $\xi=\sqrt{\pi}/\sqrt[3]{5H^3}$ because it is the optical value [25] and the sum converges very rapidly.

A nonhydrodynamic short-range repulsive force between spheres, $\boldsymbol{F}_{rep}$, is added to the system to avoid the prohibitively small time steps needed to overcome the problem of overlapping spheres. We follow Brady and Bossis [27] and Ishikawa and Pedley [22] and use the following function:

$$\boldsymbol{F}_{rep} = \alpha_1 \frac{\alpha_2 \exp(-\alpha_2 \varepsilon)}{1-\exp(-\alpha_2 \varepsilon)} \frac{\boldsymbol{r}}{r}, \tag{12}$$

where α_1 is a dimensional coefficient, α_2 is a dimensionless coefficient, and ε is the minimum separation between sphere surfaces nondimensionalized by their radii. The coefficients used in this study were $\alpha_1=0.1$ and $\alpha_2=10^3$. The minimum separation obtained with these parameters was about 10^{-4}. We did not use any repulsive forces between a sphere and a fluid particle, as the velocity on a sphere's surface is given explicitly by $\boldsymbol{U}$ and $\boldsymbol{\Omega}$, which does not permit a fluid particle to penetrate into the sphere.

Considering the linearity of the Stokes flow, it is possible to split the velocity field generated by interacting spheres with repulsive forces into (a) the velocity field generated by spheres with repulsive forces in a fluid otherwise at rest and (b) the velocity generated by the other boundary conditions and force-torque conditions. Velocity (b) has been derived in Sec. II B, and velocity (a) generated by two particles in the far field can be calculated as follows. If ε is sufficiently small, the hydrodynamic stress is approximately zero everywhere except near the contact point where concentrated contact forces exist. Taking into account that the contact forces $\boldsymbol{F}_c$ on two sphere surfaces act in the opposite direction with the same absolute value, the velocity at $\boldsymbol{r}$ generated by the contact forces at the origin can be approximated as

$$u_i(\boldsymbol{r}) = -\frac{1}{8\pi\mu}\left\{ J'_{ij}\left(\boldsymbol{r}-\frac{\boldsymbol{h}_\varepsilon}{2}\right) - J'_{ij}\left(\boldsymbol{r}+\frac{\boldsymbol{h}_\varepsilon}{2}\right)\right\} F_{c,j}, \tag{13}$$

where $\boldsymbol{h}_\varepsilon$ is the separation vector between the two sphere surfaces at the contact point with the length of ε. By substituting Eqs. (8) and (12) with $\alpha_1=0.1$, it can be derived that $u=\mathcal{O}(\frac{1}{80\pi r^2})$ for large r. As this velocity is very small when r is large, the effect of repulsive force in the far field on the trajectories of fluid particles is also very small. Velocity (a) generated by two particles in the near field can be calculated again by the boundary element method, and so we compiled a database prior to the simulation in a similar manner as explained in Sec. II B.

Time-marching is performed by the fourth-order Adams-Bashforth scheme from random initial positions and orientations of both spheres and fluid tracers. The translational displacement is calculated by $\boldsymbol{U}$ as $\boldsymbol{r}=\int \boldsymbol{U}\, dt$, so the trajectories are traced outside the periodic cell. Most of the results shown in this paper were obtained using 80 spheres and 80 fluid particles per unit cell. The effect of particle number on the diffusivity was examined numerically, and the results are shown in Sec. III C. The computations are performed during a time interval of $t=0-500$ or more, and the suspension average values are calculated by averaging all particles in the unit cell from $t=50$ to the end. It was confirmed that the probability density function for the relative position of a pair of spheres becomes independent of specific initial conditions after $t=50$. All equations are nondimensionalized using the radius a, characteristic time $\dot{\gamma}^{-1}$, and the fluid viscosity μ. All quantities shown in figures in this paper are also nondimensionalized in the same manner.

D. Translational diffusivity

The translational diffusivity is a measure of the increasing displacement between pairs of particles. Thus, we calculate the mean-square displacement, which necessarily increases with time. If it increases more rapidly than linearly in time, then the spread is superdiffusive (if proportional to t^2, then the relative velocity of two particles is constant), but if it becomes linear in time, then the spread is diffusive. Thus, we divide the mean-square displacement by time to determine whether it becomes constant: the translational diffusivity $\boldsymbol{D}$ is defined by

$$\boldsymbol{D} = \int_0^\infty \langle \boldsymbol{U}(t)\boldsymbol{U}(0)\rangle dt = \lim_{\Delta t\to\infty} \frac{\langle [\boldsymbol{r}(\Delta t) - \boldsymbol{r}(0)][\boldsymbol{r}(\Delta t) - \boldsymbol{r}(0)]\rangle}{2\Delta t}, \tag{14}$$

where $\boldsymbol{r}$ is the translational displacement. The angular brackets $\langle \cdots \rangle$ indicate an average value over N particles with M different time steps, which is defined as

$$\langle \boldsymbol{r}(\Delta t) - \boldsymbol{r}(0)\rangle = \frac{1}{MN}\sum_{m=1}^{M}\sum_{n=1}^{N} \boldsymbol{r}_n(\Delta t + mdt) - \boldsymbol{r}_n(mdt), \tag{15}$$

where dt is the time step used in the numerical simulation.

III. BENCHMARK TESTS OF THE PRESENT NUMERICAL METHODS

In this section, we examine the reliability of the present numerical methods in three different cases: (a) comparison of velocity field around a single sheared sphere between the present methods and the exact solution, (b) comparison of the velocity field around two sheared spheres between the present methods and BEM, and (c) comparison of the diffusivities obtained by the present methods using different particle numbers. In comparison (a), the accuracy of the near- and far-field approximation in the velocity field can be determined. Comparison (b) allows examination of the reliability of the velocity field between two near-contact surfaces. In comparison (c), the effect of the particle number on the diffusivity can be determined.

A. Velocity around a single sheared sphere

The velocity field around a single sphere freely suspended in a simple shear flow was compared between the present method and the exact solution [3]. As shown in Fig. 3(a), a single sphere was placed at the origin and background shear was applied in the x-y plane. x and y components of the velocity were calculated along the $x=1.1$ line, and the results are shown in Fig. 3(b). Both velocities calculated by the present methods and the exact solution agreed very well. As explained in Sec. II B, we employed a threshold distance of 4.0 for approximation of far-field interactions. Thus, the velocity of the present study was calculated differently depending on whether $r>4$. The boundary is shown explicitly in Fig. 3(b) as thin solid lines at $y \approx \pm 3.8$. In the near field, the velocity is interpolated from the database compiled by the BEM. The velocity in the far field was calculated using a small number of multipoles. Our results confirmed that the near- and far-field approximations are sufficiently accurate.

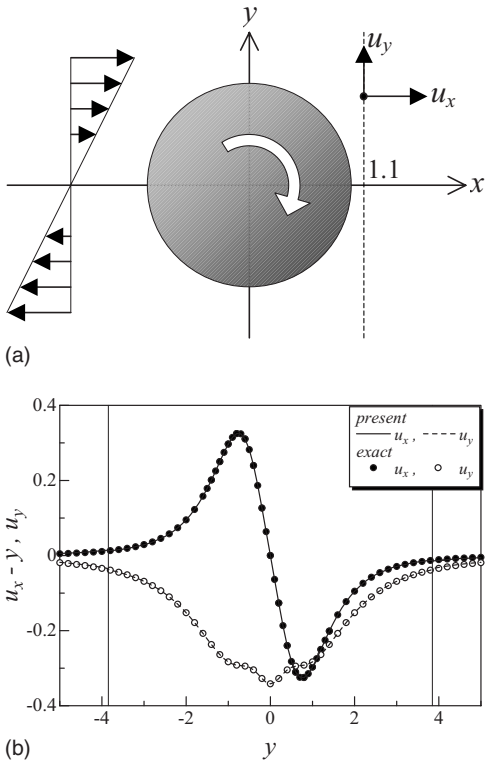

FIG. 3. Velocities around a single sheared sphere. (a) Schematic representation of the computed system. (b) Comparison of velocity distribution between the present method (*present*) and the boundary element method (*BEM*).

B. Velocity around two sheared spheres

The velocity field around two spheres freely suspended in a simple shear flow was compared between the present method and the boundary element method [21]. As shown in Fig. 4(a), two spheres were aligned on the x axis with a gap of 0.2. The x and y components of the velocity were calculated along the y axis, and the results are shown in Fig. 4(b). Again, the velocities calculated by both the present methods and the BEM agreed very well. In the near field, the velocity was interpolated from the database compiled by the BEM. Our results confirmed that the near-field interpolation is sufficiently accurate even in the two-sphere case.

C. Effect of the particle number on the diffusivity

To clarify the effects of particle number on the diffusivity of fluid tracers, we computed the diffusivity with changes in the number of both spheres and fluid tracers to 60, 80, and 100. Since we took the radius a as the characteristic length, increasing the number of spheres under the constant volume fraction corresponds to expanding the unit computational cell size. The results of D_{yy} and D_{zz} are shown in Fig. 5 ($c=0.1$). The effect of particle number was not highly significant. In the present study, we employed a hexahedron of

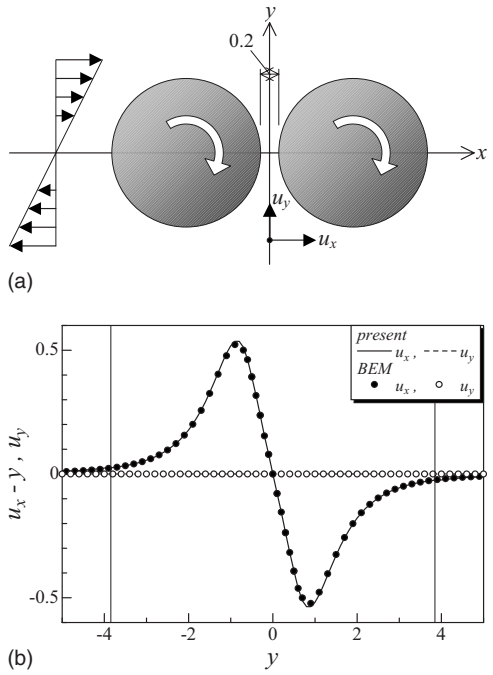

FIG. 4. Velocities around two sheared spheres.

dimension $5H \times H \times H$ as a unit computational cell (see Fig. 2). By increasing the x length slightly from a cubic unit cell, we could calculate diffusivity more accurately under conditions of a fixed particle number. This was because spheres in a shear flow move in the x direction and the number of collisions between spheres increases as the x length of the unit cell is increased. This leads to a spreading of spheres and configuration changes in the system, and eventually to diffusion of spheres. Thus, we employed the hexahedron unit cell in the present study. In the following computations, we placed 80 spheres and 80 fluid particles per unit cell.

IV. RESULTS

The movements of 80 spheres and fluid tracers in a simple shear flow field were computed under the condition $c=0.1$.

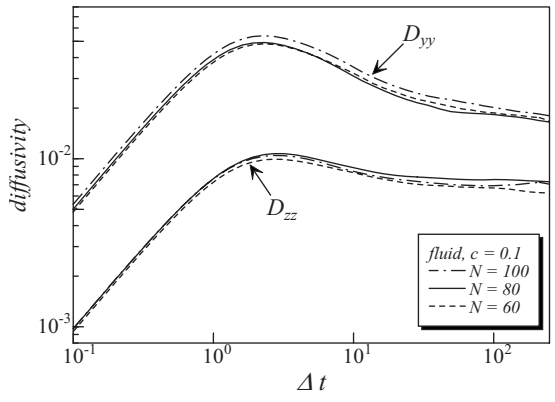

FIG. 5. Effects of particle number on the diffusivity of fluid tracers, where N is the number of both spheres and fluid tracers. (a) Instantaneous positions of 80 spheres and trajectories of the spheres during one time interval. (b) Trajectories of the fluid tracers during one time interval.

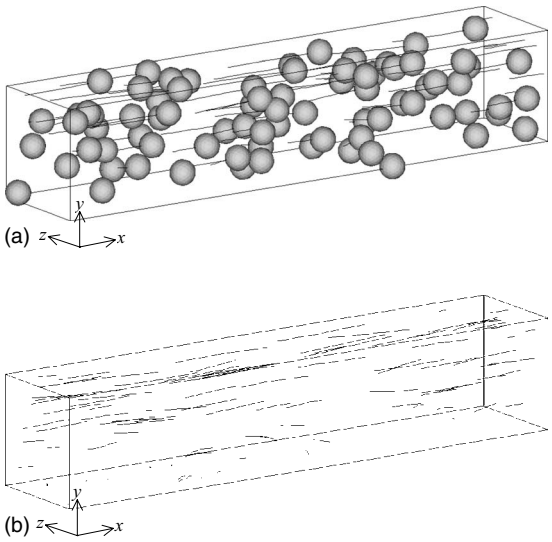

FIG. 6. Trajectories of spheres and fluid tracers in a sheared suspension with $c=0.1$. The background simple shear flow is in the x-y plane. (a) Square displacement of spheres. (b) Square displacement of fluid tracers.

The instantaneous positions of spheres and their trajectories during one time interval are shown in Fig. 6(a), where the background shear flow is in the x-y plane. Some of the lines in Fig. 6(a) are not attached to spheres because a sphere passing through the boundary of the periodic cell is replaced on the other side and its trajectory shows a jump at the boundary. As the background translational velocity increases with y, the trajectories of spheres in high-y positions become longer than those in low-y positions. The spheres in a shear flow cannot move in straight lines because of hydrodynamic interactions between them. Figure 6(b) presents the trajectories of fluid tracers during one time interval. As shown in the figure, fluid tracers also do not move in straight lines because the interacting spheres generate a complex flow field around them.

To discuss the spreading characteristics, the mean-square displacements of spheres and fluid tracers were calculated. Figure 7 shows the results of $c=0.1$, where $\Delta r_i = r_i(\Delta t) - r_i(0)$ and $\Delta r_x'$ is the displacement relative to the background shear field defined as $\Delta r_x' = \int_0^{\Delta t} U_x - y \, dt$. Solid lines with slope 1 and dashed lines with slope 2 have been added in the figure for comparison. When $\Delta t \leq 1$, all square displacements fit well with the dashed lines, indicating that the relative velocity of two particles was constant over this short time interval. However, when $\Delta t \geq 100$, all square displacements fit well with the solid lines, indicating that the spread was diffusive over this long time interval. Thus, the spreading of both spheres and fluid tracers can be described correctly as a diffusive process over a sufficiently long time scale, even though all the movements were calculated deterministically.

Diffusivity can be calculated from the square displacement by Eq. (14). The D_{yy} of spheres with various volume fractions c are shown in Fig. 8(a). As indicated in the figure, D_{yy} increases as c is increased because the hydrodynamic interaction between spheres increases with c. This tendency is consistent with previous studies [10,12,13], in which in-

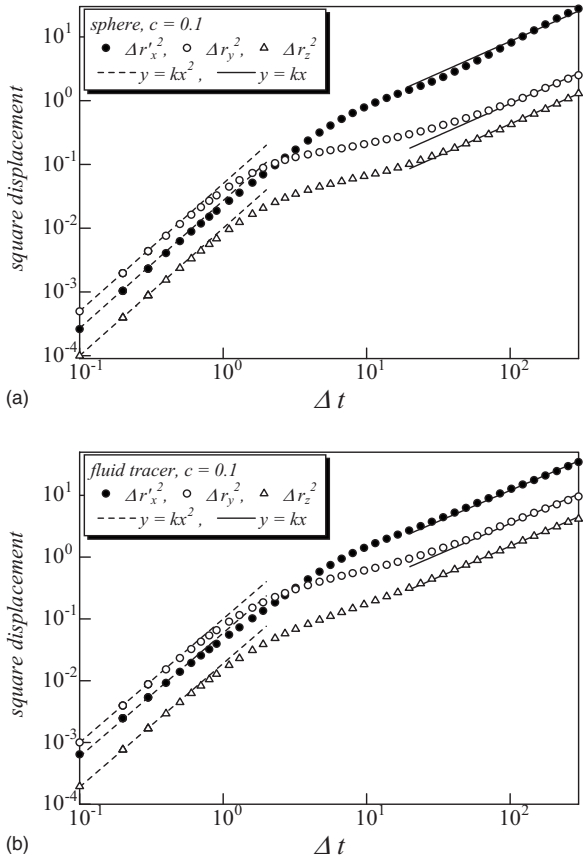

FIG. 7. Ensemble square displacements of spheres and fluid tracers during time interval Δt. Dashed lines have slope 2, and solid lines have slope 1. $\Delta r_x'$ is the displacement in the x direction relative to the background shear field. (a) D_{yy} of spheres. (b) D_{yy} of fluid tracers.

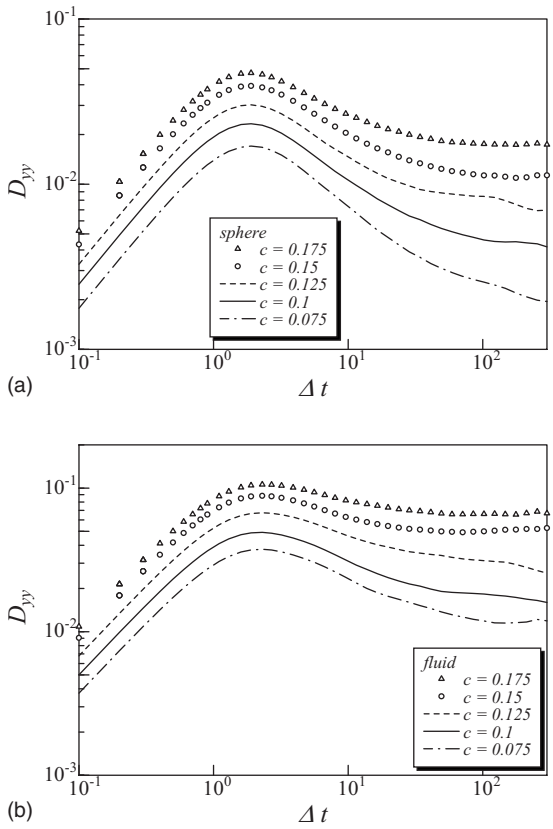

FIG. 8. Effects of the volume fraction on the yy component of the diffusivity. (a) D_{zz} of spheres. (b) D_{zz} of fluid tracers.

creases in D_{yy} were observed up to $c \approx 0.4$. D_{yy} of fluid tracers also increases as c is increased, as shown in Fig. 8(b). Moreover, the D_{yy} of fluid tracers is slightly larger than that of spheres. This tendency is different from that reported previously by Breedveld *et al.* [17], in which D_{yy} of fluid tracers was about 0.7 times that of spheres. The reason for this will be discussed in Sec. V.

Figure 9(a) shows D_{zz} values of spheres with various volume fractions. Again, D_{zz} increased with increasing c, consistent with previous studies in which increases in D_{zz} were observed up to $c \approx 0.5$ [10,12]. In these previous studies, D_{zz} was about half of D_{yy} under conditions of fixed c, which was also observed in the present study. D_{zz} of fluid tracers again increased with increasing c, as shown in Fig. 9(b). Consistent with the present results, Breedveld *et al.* reported that D_{yy} of fluid tracers is about 1.7 times D_{zz} [17]. However, the D_{zz} of fluid tracers was slightly larger than that of spheres in the present study, which was different from the tendency reported by Breedveld *et al.* [17].

V. DISCUSSION

The previous section discussed diffusivity of fluid tracers with $c=0.075-0.175$. The main difference between our results and those of the previous experimental study of Breedveld *et al.* [17] is that the diffusivity of fluid tracers was shown to be larger than that of spheres. This may have been due to differences in the volume fraction used between the two studies; Breedveld *et al.* used a suspension with $c=0.3-0.5$, which was much denser than that in the present study. Under the dilute regime, we clearly showed that the diffusivity of fluid tracers becomes larger than that of spheres. In fact, Zarraga and Leighton [15] and Abbas *et al.* [16] reported that the diffusivity of small spheres is higher than the large spheres in bidisperse suspensions, which supports our findings.

In the dilute limit, we can assume that the interaction between spheres is pairwise and the other spheres have no major effect on this interaction. Due to the background shear flow in the x-y plane, two spheres initially at $(-1.5,1,0)$ and $(1.5,-1,0)$ move along the trajectories shown in Fig. 10(a) and finally reach the black circles at $(1.5,1,0)$ and $(-1.5,-1,0)$. These trajectories were calculated by the present methods and were consistent with the analytical results derived by Batchelor and Green [3] and Kim and Karrila [28]. As the trajectories are symmetric in the y direction, no net displacement of spheres in the y direction occurs during the interaction—i.e., $\Delta r_y=0$. Thus, no diffusivity of spheres exists in the y direction in the dilute limit assuming pairwise interactions (cf. Acrivos *et al.* [4]). The same is true for net displacement in the z direction; in the dilute limit, no diffusivity of spheres takes place in the z direction.

In the case of fluid tracers, however, diffusivity does appear in the above case. Fluid tracers were initially placed

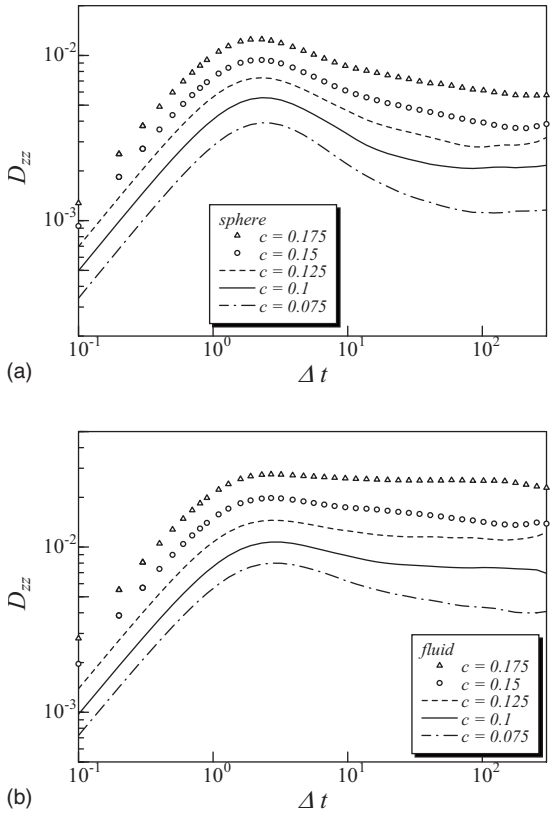

FIG. 9. Effects of the volume fraction on the zz component of the diffusivity. (a) Trajectories of two spheres in a shear flow, where spheres move from gray circles to black circles. (b) Trajectories of fluid tracers around two sheared spheres.

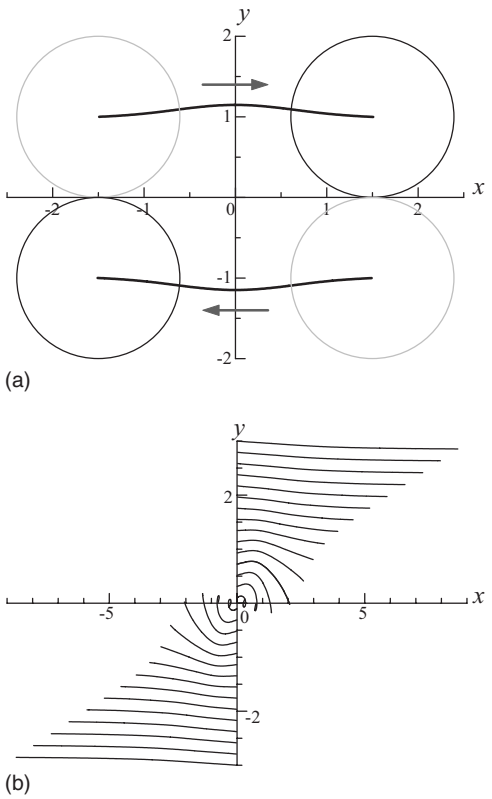

FIG. 10. Trajectories of spheres and fluid tracers in a shear flow. Initially two spheres are placed in the black circles in (a) and the fluid tracers are placed along the y axis. Trajectories are calculated until two spheres reach the black circles in (b).

along the y axis, and their subsequent trajectories are shown in Fig. 10(b). Their movements were calculated while two spheres moved from the gray to the black circles in Fig. 10(a). The fluid tracers could be seen to move considerably in the y direction as well as the x direction, even though the trajectories of the two spheres were symmetrical as shown in Fig. 10(a). Thus, the diffusivity of fluid tracers appears even in the dilute limit assuming pairwise interaction of spheres. This may be the reason why the diffusivity of fluid tracers is greater than that of spheres under the semidilute regime.

Discussing scaling of the diffusivity of fluid tracers is also important. The probability of a fluid tracer having one sphere in its near field is $\mathcal{O}(c)$. Therefore, we first examined whether fluid tracers diffuse as $\mathcal{O}(c)$. Let a solitary sphere be at the origin and apply the background shear flow as in Eq. (11). The velocity at $\boldsymbol{r}$ around the sphere under force- and torque-free conditions is given as follows (cf. Batchelor and Green [3]):

$$u_i(\boldsymbol{r}) = E_{ij}r_j + \epsilon_{ijk}\omega_j r_k + E_{jk}r_j\left[-\frac{\delta_{ik}}{r^5} + \frac{r_i r_k}{r^2}\left(-\frac{5}{2r^3} + \frac{5}{2r^5}\right)\right]. \tag{16}$$

This equation indicates that the trajectories of fluid tracers relative to the sphere are symmetric and no net displacement occurs in the y or z directions during the interaction. Therefore, the diffusivity of fluid tracers does not appear in the single-sphere case and it is not $\mathcal{O}(c)$.

As discussed in Fig. 10, fluid tracers do diffuse during the pairwise interaction of spheres. As the probability of a fluid tracer having two spheres in its near field is $\mathcal{O}(c^2)$, the diffusivity should also be $\mathcal{O}(c^2)$. To confirm this tendency, we plotted c versus diffusivities averaged over $\Delta t = 100-300$ on a log-log scale, as shown in Fig. 11. We can see that both D_{yy} and D_{zz} fit well with the solid lines with slope 2. D_{yy} is about threefold greater than D_{zz}. We therefore confirmed that the diffusivity of fluid tracers increases as $\mathcal{O}(c^2)$ under the semidilute regime.

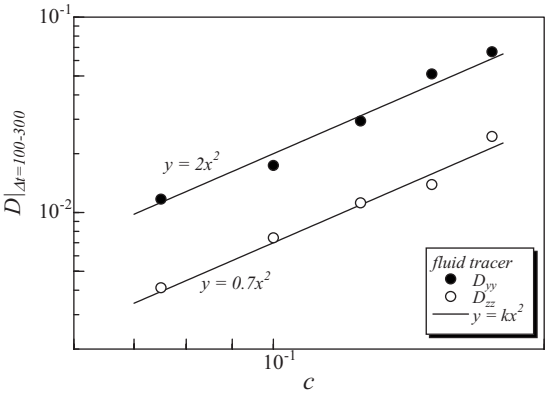

FIG. 11. Scaling of D_{yy} and D_{zz} of fluid tracers averaged over $\Delta t = 100-300$. Solid lines have slope 2.

Last, we discuss effects of the self-diffusion due to the Brownian motion, which may appear in the case of practical fluid. The self-diffusivity of H_2O molecules in a still water is about 5×10^{-10} m^2 s^{-1} at room temperature [29]. We should note that the self-diffusivities of other liquids are not much different [18]. Such self-diffusion is generated by the Brownian motion of molecules, which is neglected in the present study. In order to compare the self-diffusivity of H_2O with the present results of the fluid-tracer diffusivity, we nondimensionalize it by using the radius a and characteristic time $\dot{\gamma}^{-1}$. When $5\times10^{-10}/(a^2\dot{\gamma})\ll D$, the Brownian effect can be neglected compared to the shear-induced diffusivity. When $5\times10^{-10}/(a^2\dot{\gamma})\gg D$, on the other hand, the diffusion is mainly generated by the Brownian motion and the effect of shear flow can be neglected. If we approximate, the shear-induced fluid-tracer diffusivity is about c^2 (cf. $D_{yy}=2c^2$ and $D_{zz}=0.7c^2$); as shown in Fig. 11, the shear-induced diffusivity becomes significant when $5\times10^{-10}<a^2\dot{\gamma}c^2$.

ACKNOWLEDGMENTS

This study was supported in part by a Grant-in-Aid for Young Scientists (A) from the Japan Society for the Promotion of Science (JSPS), No. 19686016, and by a Grant-in-Aid for Scientific Research (S) from JSPS, No. 19100008. We are also grateful for the support of the Tohoku University Global COE Program, Nano-Biomedical Engineering Education and Research Network Centre.

[1] A. S. Ahuja, W. R. Hendee, and P. L. Carson, Phys. Med. Biol. **23**, 928 (1978).
[2] Xiao-Lun Wu and A. Libchaber, Phys. Rev. Lett. **84**, 3017 (2000).
[3] G. K. Batchelor and J. T. Green, J. Fluid Mech. **56**, 375 (1972).
[4] A. Acrivos, G. K. Batchelor, E. J. Hinch, D. L. Koch, and R. Murai, J. Fluid Mech. **240**, 651 (1992).
[5] Y. Wang, R. Murai, and A. Acrivos, J. Fluid Mech. **357**, 279 (1998).
[6] M. Marchioro and A. Acrivos, J. Fluid Mech. **443**, 101 (2001).
[7] G. Drazer, J. Koplik, B. Khusid, and A. Acrivos, J. Fluid Mech. **460**, 307 (2002).
[8] J. F. Morris and J. F. Brady, J. Fluid Mech. **312**, 223 (1996).
[9] J. F. Brady and J. F. Morris, J. Fluid Mech. **348**, 103 (1997).
[10] D. Foss and J. F. Brady, J. Fluid Mech. **401**, 243 (1999).
[11] D. Foss and J. F. Brady, J. Fluid Mech. **407**, 167 (2000).
[12] A. Sierou and J. F. Brady, J. Fluid Mech. **506**, 285 (2004).
[13] E. C. Eckstein, D. G. Bailey, and A. H. Shapiro, J. Fluid Mech. **79**, 191 (1977).
[14] A. Acrivos, J. Rheol. **39**, 813 (1995).
[15] I. E. Zarraga and D. T. Leighton, Jr., J. Colloid Interface Sci. **243**, 503 (2001).
[16] M. Abbas, E. Climent, O. Simonin, and M. R. Maxey, Phys. Fluids **18**, 121504 (2006).
[17] V. Breedveld, D. V. D. Ende, A. Tripathi, and A. Acrivos, J. Fluid Mech. **375**, 297 (1998).
[18] J. C. M. Li and P. Chang, J. Chem. Phys. **23**, 518 (1955).
[19] G. K. Youngren and A. Acrivos, J. Fluid Mech. **69**, 377 (1975).
[20] J. F. Brady and G. Bossis, Annu. Rev. Fluid Mech. **20**, 111 (1988).
[21] T. Ishikawa, M. P. Simmonds, and T. J. Pedley, J. Fluid Mech. **568**, 119 (2006).
[22] T. Ishikawa and T. J. Pedley, J. Fluid Mech. **588**, 399 (2007).
[23] T. Ishikawa and T. J. Pedley, J. Fluid Mech. **588**, 437 (2007).
[24] T. Ishikawa, J. T. Locsei, and T. J. Pedley (unpublished).
[25] C. W. J. Beenakker, J. Chem. Phys. **85**, 1581 (1986).
[26] L. Durlofsky, J. F. Brady, and G. Bossis, J. Fluid Mech. **180**, 21 (1987).
[27] J. F. Brady and G. Bossis, J. Fluid Mech. **155**, 105 (1985).
[28] S. Kim and S. J. Karrila, *Microhydrodynamics: Principles and Selected Applications* (Butterworth Heinemann, London, 1992).
[29] J. H. Wang, J. Am. Chem. Soc. **73**, 4181 (1951).